Chemical Engineering Journal 518 (2025) 164789

Contents lists available at ScienceDirect

Chemical Engineering Journal

journal homepage: www.elsevier.com/locate/cej

Basal and edge plane activity of two-dimensional Dirac semimetal $NiTe_2$ for hydrogen evolution reaction

Seung Weon Jeong [a,1], Jeong Hyo Kim [a,1], Seungyeon Lee [a], Hyeonju Kim [a], Hee Jung Park [b], Heejun Yang [c], Sangheon Lee [a,*], Suyeon Cho [a,*]

[a] Division of Chemical Engineering and Materials Science, Graduate Program in System Health Science and Engineering, Ewha Womans University, Seoul 03760, Republic of Korea
[b] Metropolitan Seoul Center, Korea Basic Science Institute, Seoul 03759, Republic of Korea
[c] Department of Physics, Korea Advanced Institute of Science and Technology (KAIST), Daejeon 34141, Republic of Korea

ARTICLE INFO

Keywords:
Hydrogen evolution reaction
HER microreactor
Nickel telluride
Topological semimetal

ABSTRACT

Nickel ditelluride ($NiTe_2$), one of the group-10 transition metal dichalcogenides, has shown intriguing surface states originating from its topological semimetallicity. Here, we demonstrate abnormal catalytic activities at the $NiTe_2$ surface for the hydrogen evolution reaction (HER). We investigate the differences in catalytic activities at the basal and edge planes of $NiTe_2$ using a micro-sized electrochemical reactor. The basal plane is found to be more active than the edge plane, resulting in a current density at the basal plane of $NiTe_2$ exceeding 700 mA/cm^2 with a small overpotential of −0.162 V. Interestingly, our ab initio calculations show a discrepancy with the experimental measurements, indicating that the crystal-orientation-dependent HER activity highlights the unique characteristics of a topological semimetal, which can significantly influence the HER in $NiTe_2$ catalysts.

1. Introduction

Recent advances in two-dimensional (2D) catalysts have significantly enhanced hydrogen evolution reaction (HER) performance through innovative structural and electronic engineering strategies [1–8]. Fundamental and thorough research has been conducted on two-dimensional (2D) catalysts, demonstrating a trend toward rational, multiscale design of 2D catalysts driven by experimental and data-driven approaches [9,10]. These catalysts have been of great interest because of their exotic physics and chemistry, which can be applied to next-generation catalysis [5–8]. Some 2D catalysts are even considered topological catalysts, possessing high current density and carrier mobility, which can lead to improved and sustained catalytic performance [11–14]. However, a detailed understanding of the mechanisms behind the exceptional performance of these topological catalysts is still needed.

Among 2D catalysts, group-10 transition metal dichalcogenides (TMD) such as PdS_2, $PdSe_2$, PtS_2, and $PtSe_2$ have attracted considerable attention because group-10 noble metals such as Pd and Pt have shown outstanding catalytic activities [15–17]. In group-10 TMDs, most TMD compounds with S and Se are semiconductors, whereas TMDs with Te are semimetals. Meanwhile, group-10 transition metal ditellurides such as $PdTe_2$ and $PtTe_2$ showed better catalytic activities for various electrochemical reactions than other group-10 TMDs with S and Se [18]. In the case of nickel-chalcogen compounds, Ni ions not only increase the free energy density but also provide abundant reactive sites [19,20]. Because Te ions have higher metallic properties and lower electronegativity than other sulfides (O, S, and Se) [21,22], introducing Te ions in $NiTe_x$ could optimize electron states, enhance conductivity, and further improve the electrochemical performance of HER [23,24].

Nickel ditelluride ($NiTe_2$) has been reported as a type II Dirac semimetal exhibiting topological surface states with many Dirac points near the Fermi level. It has been less studied in catalysis than other group-10 TMDs so far [25,26]. Many researchers have reported that the outstanding surface transport of Dirac/Weyl fermions of topological semimetals can enhance the catalytic activity at the surface for electrochemical reactions with theoretical and experimental evidence [27–30]. Many studies have proven that the topological surface state is symmetry-protected and robust against adsorbents, defects, oxidation, or reduction at the surface, opening a new era of highly efficient 2D

* Corresponding authors.
E-mail addresses: sang@ewha.ac.kr (S. Lee), s.cho@ewha.ac.kr (S. Cho).
[1] These authors contributed equally to this work.

https://doi.org/10.1016/j.cej.2025.164789
Received 19 February 2025; Received in revised form 25 May 2025; Accepted 11 June 2025
Available online 16 June 2025
1385-8947/© 2025 The Authors. Published by Elsevier B.V. This is an open access article under the CC BY license (http://creativecommons.org/licenses/by/4.0/).

catalysts for next-generation energy conversion. However, the study on how the remarkable transport properties of topological semimetals contribute to the catalytic properties still needs further investigation.

Recently, Zhang et al. reported that topological surface state density at the Fermi level can be a universal catalytic descriptor for electrocatalytic reactions in the family of metal diborides. The (001) and (010) surfaces of metal diborides exhibit different catalytic activities because of different topological surface state densities [31]. Considering the anisotropy of charge transport in topological semimetals, topological semi-metallicity-driven electrocatalytic activities of topological semimetals must be analyzed with surface-orientation dependency. However, electrochemical reactions conventionally measure the average properties of massive catalysts. Therefore, the atomistic mechanism behind the distinct reactivity of basal- and edge-plane atoms of 2D materials has to be investigated by analyzing crystal-orientation-sensitive activity for HER.

Various synthesis methods have been employed to grow high-quality single crystals of $NiTe_2$, and the intrinsic properties of $NiTe_2$ have been studied so far [32–36]. For practical application to catalysts, nanoparticulate $NiTe_2$ with porous geometry has been demanded. Therefore, hydrothermal or electrochemical synthesis on foam or mesh substrates has been suggested [37,38]. Some HER studies with nanoparticulate $NiTe_2$ have been reported so far. However, the inherent HER of $NiTe_2$ has not been experimentally investigated with atomic-level analysis.

Here, we study the catalytic activity of $NiTe_2$ flakes for active HER with different surface morphologies, bumpy and flat surfaces. $NiTe_2$ flakes are synthesized by tellurizing a Ni thin film, which is pre-deposited on a SiO_2/Si substrate, using a two-zone furnace method. Flat $NiTe_2$ flakes are synthesized through high-temperature synthesis with a lateral size of 20 μm. In contrast, a porous sample geometry and a lateral size of 2 μm are obtained by low-temperature synthesis. The crystal structure of the flat $NiTe_2$ is well-aligned along the *c*-axis, showing strong 2D characters. We also examine the HER activity of the basal plane and edge atoms of flat and porous $NiTe_2$ flakes using an HER microreactor with selectively opened HER windows to the electrolyte. The HER microreactor is designed as a micro-sized electrochemical cell fabricated by e-beam lithography. The HER activity measured from the selective sample areas of the $NiTe_2$ surface shows that the basal plane atoms have better catalytic activity than the edge atoms. The current density at the $NiTe_2$ surface of >800 mA/cm^2 can be explained by the topological behaviors of the 2D catalysts, which often show extremely large current densities in recent studies [39–41]. We also perform a series of ab initio calculations to estimate the intrinsic catalytic activities of HER on the basal and edge planes of $NiTe_2$. The observed abnormal catalytic activities at the $NiTe_2$ surface probably provide a new concept of topological catalysts for next-generation HER nanocatalysts.

2. Experimental

2.1. Sample synthesis

Ni films are deposited on clean SiO_2/Si substrates (with a SiO_2 thickness of 300 nm) using a radio frequency (RF) magnetron sputter with a Ni target (99 % purity). Commercial Ar (99.9 % purity) is used as the sputtering gas at a flow rate of 20 sccm. Before deposition, the Ni target is pre-sputtered in an Ar atmosphere for 2 min to remove any oxide layers. The films are deposited on the substrates at room temperature for 28 min. Two-dimensional $NiTe_2$ flakes are grown on Ni film substrates (with a Ni thickness of 100 nm) using a two-zone tubular furnace. Tellurium powder (Sigma Aldrich, $\geq$ 99.8 %) in a ceramic boat is placed in the upstream zone. The Ni-sputtered substrate is placed face down on a ceramic boat in the middle of the second temperature zone. Before heating, the system is purged with Ar gas to completely remove oxygen and moisture from the quartz tube. Next, the first zone (T1) and the second zone (synthetic temperature, T_{syn}) are separately heated up to 635 °C and 700 °C under a constant argon flow of 150 sccm. The temperatures are then held for 15 min in the flow of mixed gases of 5 sccm H_2 and 150 sccm Ar. After a 15-min growth period, the heating is terminated, and the furnace is opened immediately for quenching. Then, the furnace is naturally cooled to room temperature with only an Ar gas supply.

2.2. Sample characterization

For the chemical analysis of the CVD-grown $NiTe_2$ surface, X-ray photoemission spectroscopy (XPS; Thermo Scientific, U.K.) is conducted at the Yonsei Center for Research Facilities (YCRF). The base pressure is 2.9×10^{-9} mbar, and the photon energy is 1486.6 eV (Al Kα). The chemical states of our $NiTe_2$ are studied after a mild Ar-ion etching process (0.2 keV, 10 s.). The intensities of the O 1 *s* and C 1 *s* spectra decrease, and those of Ni 2*p*, Te 3*d*, and the valence band increase after the mild etching process. This indicates that the surface adsorbents, such as carbon oxides or hydroxides at the $NiTe_2$ surface, are partially removed after the mild etching process. The binding energy (BE) calibration was performed using the Fermi edge of $NiTe_2$.

The surface morphology analysis of $NiTe_2$ is performed using a field-emission scanning electron microscopy (FE-SEM) system (Hitachi SU8220 FE-SEM with a base pressure of $\sim 1 \times 10^{-8}$ Torr) equipped with an energy dispersive spectrometry (EDS) system at the Metropolitan Seoul Center, Korea Basic Science Institute.

X-ray diffraction (XRD) of $NiTe_2$ flakes is taken using an X-ray diffractometer (D/MAX-2500/PC, Rigaku, Japan) with Cu K radiation ($\lambda = 1.54060$ Å) at room temperature at the Metropolitan Seoul Center, Korea Basic Science Institute. Raman spectroscopy measurements are also performed (XperRAM C series, Nanobase) with a wavelength of 532 nm for laser excitation. We used the excitation laser with a power of <1 mW to prevent sample damage while recording the Raman spectra. All the Raman peaks are calibrated using the Raman peak of Si located at 520 cm^{-1}.

2.3. HER microreactor fabrication

HER microreactors are fabricated to measure the electrochemical properties of $NiTe_2$. First, samples are spin-coated with poly (methyl methacrylate) (PMMA), after which the areas excluding unnecessary parts of the samples are removed by photolithography. Finally, thermal evaporation is used to deposit Cr/Au (5 nm/50 nm) electrodes on the SiO_2/Si substrate (with a SiO_2 thickness of 300 nm). The CVD-grown $NiTe_2$ flakes on the SiO2/Si substrate are transferred directly onto pre-patterned Cr/Au electrodes on the SiO_2/Si substrate by a dry transfer method. PMMA is then spin-coated to cover the $NiTe_2$ and electrodes on the SiO_2/Si substrate. PMMA windows are developed to expose the target areas of the $NiTe_2$ by photolithography. The transfer process starts with preparing a polycarbonate (PC) solution by dissolving PC particles into chloroform (99.8 %) for a mass fraction of ~8 %. PC curing is performed by drop-casting the liquid PC on the glass slide and waiting until it can be solidified into a PC film. Then, we take a new glass slide where a small piece of polydimethylsiloxane (PDMS) is placed. The PC film is removed from its glass slide using adhesive tape and laid across the PDMS, acting as a stamp during the following transfer procedure. Then heat the stage to between 80 °C and 120 °C, and as the SiO_2 heats up, the contact area with the PC gradually increases further. The PC film can be easily peeled off with 2D flakes remaining on the SiO_2 substrate. After positioning the 2D sample at the targeted area, the stage temperature is elevated to 180 °C to melt the PC film on the microreactor. Finally, chloroform removes the residual PC film, leaving the $NiTe_2$ flakes in the targeted position within the microreactor.

2.4. Electrochemical measurements

A graphite rod (CE) and Ag/AgCl (RE) are used, whereas the Cr/Au electrode pattern is connected to the probe tip as a working electrode

(WE). A drop of 0.5 M of sulfuric acid (H_2SO_4) electrolyte solution is applied to the exposed PMMA window, where CE and WE are in contact with the electrolyte. A Keithley 4200 device is used to apply the voltage, which ranges from −0.5 to 1.3 V versus the RHE with steps of 5 mV/s, to evaluate the HER performance. The resulting current is measured during the HER process.

2.5. Density-functional theory (DFT) calculations

First-principles calculations are conducted within the Perdew–Burke–Ernzerhof exchange-correlation functional, as implemented in the Vienna Ab initio simulation package [42,43]. The projector-augmented wave method with a plane-wave basis set describes the interaction between the ion cores and the valence electrons. An energy cut-off of 400 eV is applied to expand the electronic eigenfunctions. The surface slab structure is vertically separated from its periodic images using a vacuum space of 15 Å. A dipole correction is applied to all surface calculations to avoid unwanted electrostatic interaction between the periodic images along the surface's usual direction. The bottom $NiTe_2$ layers are fixed at the corresponding bulk positions. In contrast, the upper $NiTe_2$ layers are fully relaxed using the conjugate gradient method until the residual forces on all constituent atoms become smaller than 5×10^{-2} eV/Å. For the Brillouin zone integration, $(3 \times 3 \times 1)$ and $(3 \times 1 \times 1)$ Monkhorst–Pack meshes of k-points are used to determine the optimal geometries and total energy of the $NiTe_2$ (001) and $NiTe_2$ (100) surface models, respectively. Reaction pathways and barriers are determined using the climbing-image nudged elastic band (c-NEB) method for each elementary step [44].

2.6. Thermodynamic analysis

A scheme previously reported by Nörskov et al. [45] calculates the

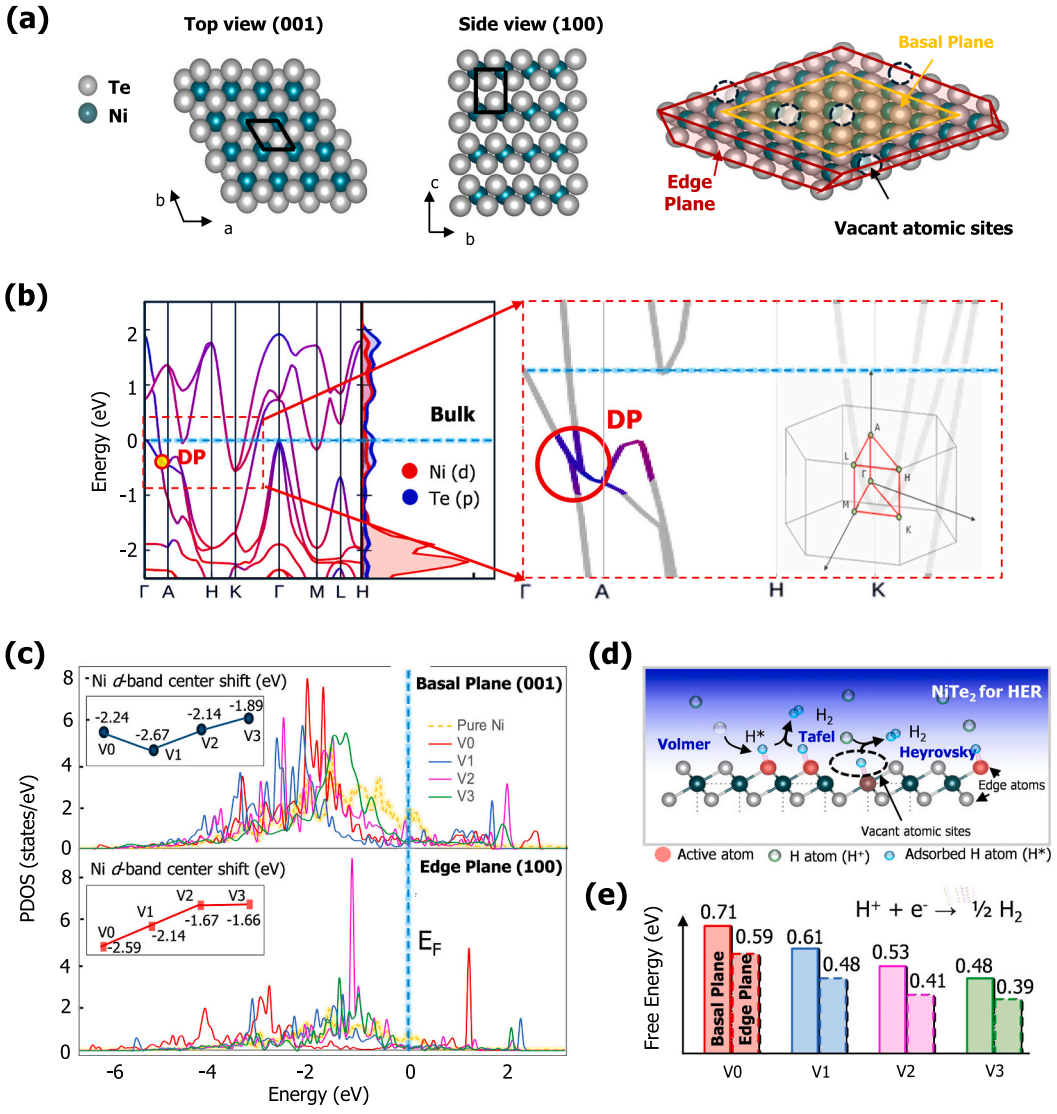


Fig. 1. (a) $NiTe_2$ with a top view (001) and a side view (100). Basal (yellow-shaded region) and edge (red-shaded region) planes of the $NiTe_2$ monolayer with vacant atomic sites. (b) Band plot and PDOS plot of bulk $NiTe_2$ near E_F. The *d* orbital of the Ni atom and the *p* orbital of the Te atom are denoted in red and blue, respectively. The Dirac point (DP) at −0.4 eV is located along Γ-A direction. (c) PDOS projected on the 4*d* orbitals of the Ni site for the basal plane (001) and edge plane (100) as a function of the number of Te vacancies; V0, V1, V2, and V3 indicate zero-, one-, two-, and three-point vacant sites, respectively. Pure Ni metal with (001) and (100) planes are added for comparison with the Ni sites in $NiTe_2$. The insets depict a variation of the *d*-band center of the Ni site as a function of the number of Te vacancies in the basal and edge planes. (d) HER with Volmer, Heyrovsky, and Tafel steps at the surface of $NiTe_2$. Possible active sites for HER can be basal-plane Te atoms, basal-plane Ni atoms near the Te vacancy, edge plane Te atoms, and edge plane Ni atoms near the Te vacancy. (e) Calculated free energies for H_2 evolution reaction ($H^+ + e^- \rightarrow H^*$) catalyzed by the basal plane (001) and edge plane (100) as a function of the number of Te vacancies (V0, V1, V2, and V3).

electrode potential and free energy of hydrogen adsorption based on the binding free energies of H* (ΔG_{H^*}) from the DFT calculations. The calculated free energy with reduction steps of Γ_1 and Γ_2 (= − Γ_1) can be directly converted into electrode potentials (E_1° and E_2°) relative to the standard hydrogen electrode (SHE), using a computational hydrogen electrode (CHE) scheme and applying the Nernst equation ($\Delta G = -nFE^\circ$, with $n = 1$, F = 1, and ΔG in eV). Therefore, the HER activity can be enhanced by decreasing the free energy of hydrogen adsorption (Γ_1) in the catalytic atoms. Here, the binding free energy of the adsorbed state is calculated as $\Gamma_1 = \Delta G_{H^*} = \Delta E_H + \Delta E_{ZPE} - T\Delta S_H$. In this equation, ΔE_H is the hydrogen adsorption energy at 0 K and 0 atm, ΔE_{ZPE} is the difference in the zero-point energy, and ΔS_H is the difference in entropy. For ΔE_{ZPE}, we take 0.04 eV as a representative value, referring to the calculated value for an H/Cu(111) system [46]. Then, the equation to calculate the binding free energy of the absorbed state is given as $\Gamma_1 = \Delta G_{H^*} = \Delta E_H + 0.24$ eV.

3. Results and discussions

$NiTe_2$ has a CdI_2-type trigonal (1T) structure with a space group of $P\bar{3}m1$. Fig. 1(a) shows that one layer of $NiTe_2$ comprises Ni atoms sandwiched by top and bottom Te atoms with octahedral coordination, and each layer of $NiTe_2$ is stacked along the *c*-axis. The $NiTe_2$ (001) surface is considered a basal plane, whereas the $NiTe_2$ (100) surface is an edge plane. We simplify that the HER process occurs at the basal plane atoms (yellow shaded area in Fig. 1(a)) and edge (red shaded area in Fig. 1(a)) plane atoms of $NiTe_2$ with four kinds of active atoms; basal plane Te atoms (Te_{BP}), basal plane Ni atoms near Te vacancy (Ni_{BP}), edge plane Te atoms (Te_{EP}), and edge plane Ni atoms near the Te vacancy (Ni_{EP}).

Fig. 1(b) shows the electronic structure and the calculated density of states (DOS) of bulk $NiTe_2$ with 1 T structure. Since the interlayer hopping is negligible, many 2D systems exhibit dispersionless energy bands in the out-of-plane k_z direction [47,48]. The electronic structure of $NiTe_2$ has a strong k_z-dispersion in the out-of-plane Γ-A direction with a unique crossing-point of the linear energy dispersion curves, which has been reported as a Dirac point (DP) of type II semimetal $NiTe_2$ [25,26,49–51]. Since topological semimetals have arisen by breaking the inversion or time-reversal symmetry, it is expected to have a considerable mixing of orbitals with different parities. Bahramy et al. reported that some TMDs with 1 T structure could be topological semimetals with Dirac points in the out-of-plane direction driven by chalcogen *p* orbitals [52]. They insisted that the p_z-derived bands (even parity) have a strong k_z-dispersion. In contrast, p_x and p_y-derived bands (odd parity) are dispersionless along the out-of-plane direction. This leads to a band crossing of 5*p* orbitals with different parities in the Γ-A direction of 1 T TMDs. Interestingly, the $NiTe_2$ exhibits the DP in the out-of-plane Γ-A direction, and the DP is mostly made of Te 5*p* orbitals, consistent with the reported type II semimetallic 1 T TMDs.

Conventional *d*-band center theory suggests that modulating the *d*-band center can enhance the electrocatalytic activity of noble and transition metal catalysts by adjusting the adsorption strength of molecules with catalysts [39]. The bulk $NiTe_2$ exhibits many dispersive energy bands crossing the E_F, mainly composed of Te 5*p* orbitals hybridized with Mo 4*d* orbitals, providing a semi-metallicity with multiple types of carriers [29]. Therefore, charge transport can be enhanced between the surface of $NiTe_2$ and adsorbed proton molecules via Mo 4*d*—Te 5*p* hybridized orbitals near E_F. Fig. 1(c) shows the calculated partial density of state (PDOS) of the Ni *d* orbital in the $NiTe_2$ and Te-deficient $NiTe_2$ surfaces. The basal plane (001) and the edge plane (100) of $NiTe_2$ exhibit the PDOS with localized *d* bands compared with the fully delocalized *d* bands of the Ni metal surface. The *d* bands in the PDOS vary with the number of Te vacancies on the $NiTe_2$ (001) and $NiTe_2$ (100) surfaces. Additionally, the PDOS near the Fermi energy increases with Te vacancies in $NiTe_2$ [53]. Overall, the $NiTe_2$ (100) surface yields a more upshifted *d* band center than the $NiTe_2$ (001) surface as the number of Te vacancies increases (see the insets of Fig. 1 (c)).

Since HER activity is tested using an acidic electrolyte (0.5 M H_2SO_4) in this study, we can expect the Volmer-Tafel mechanism or Volmer-Heyrovsky mechanism for HER, which can be analyzed based on the reaction-free energies of the two successive electrochemical reduction steps, Γ_1 ($H^+ + e^- \rightarrow H^*$) and Γ_2 ($H^* \rightarrow 1/2\ H_2$), at the $NiTe_2$ surface [54]. The proton ion (H^+) approaches the active sites such as the basal plane atoms, edge atoms, or vacant active sites (marked with red spheres in Fig. 1(d)). Then, H^+ ions turn to adsorbed H atoms (H*) at the active sites of the $NiTe_2$ surface by receiving electrons (Volmer step). The H* atom reacts with the approaching H^+ ion, resulting in an H_2 molecule by receiving an electron (Heyrovsky step), or two H* atoms meet in a surface diffusion process, resulting in an H_2 gas molecule (Tafel step). We then estimate the site-dependent HER activity by calculating the reaction-free energy (ΔG_{H^*}) of the hydrogen adsorption step (Γ_1 reduction step, $H^+ + e^- \rightarrow H^*$) for different active sites [55–58]. All four active sites (Te_{BP}, Ni_{BP}, Te_{EP}, and Ni_{EP}) yield positive ΔG_{H^*} values for both the basal and edge planes. For each plane, the Te sites have larger ΔG_{H^*} values than the Ni sites (see Table S1 in the Supplementary), indicating that the hydrogen adsorption at the $NiTe_2$ surface likely occurs at the Ni atoms in both the basal and edge planes.

Fig. 1(e) shows the calculated ΔG_{H^*} at Ni_{BP} (basal plane Ni atoms) and Ni_{EP} (edge plane Ni atoms) as a function of the number of Te vacancies. We find that for both Ni_{BP} and Ni_{EP} sites, the calculated ΔG_{H^*} values tend to decrease as the number of Te vacancies increases. In particular, for a given number of Te vacancies, the Ni_{EP} site yields a consistently lower ΔG_{H^*} value than the Ni_{BP} site. These calculation results suggest that the edge planes are likely to have higher HER activity than the basal plane and that the Ni atoms at the Te-deficient edge planes are likely active sites for the HER in $NiTe_2$.

Our theoretical analysis has focused on the hydrogen adsorption energies, central to the Volmer and Heyrovsky steps of the HER progression. To investigate the effects of the Tafel step on the overall HER activity, we perform the c-NEB simulations to characterize the surface diffusion probability of the adsorbed hydrogen atoms (H*) on the basal and edge plane of $NiTe_2$. The c-NEB simulations are designed to find the minimum energy pathway and energy barrier for the diffusion of H*. The minimum-energy path on the basal plane is from Ni to Ni. Therefore, the energy barrier is created when the H* transfers from Ni to the Te atom and from the Te atom to Ni, as shown in Fig. 2(a). We define the first energy barrier (Ni to Te) as the energy barrier of the transition state (TS) for the basal plane surface. The minimum-energy path creates an energy barrier for the edge plane surface when the H* transfers from Ni to the Te atom, as shown in Fig. 2(b). The energy barriers for the surface diffusion of H* are 0.41 eV and 0.29 eV for the basal and edge plane, respectively. This indicates that the Tafel step undergoes at the edge plane faster than the basal plane. Therefore, our theoretical predictions claim that the edge plane of $NiTe_2$ is more favorable for the HER than the basal plane, both kinetically and thermodynamically.

To experimentally study the HER process at the basal and edge planes of $NiTe_2$, we synthesized $NiTe_2$ by tellurizing a Ni thin film using the conventional CVD method. Different morphologies, a flat, sloped, or bumpy surface (see Fig. S1), of as-prepared $NiTe_2$ flakes have been employed to study the HER with basal-plane-rich or edge-plane-rich conditions. The detailed synthetic conditions are described in the methods. The sample morphologies of the CVD-grown $NiTe_2$ flakes with different synthetic temperatures (T_{syn}) are checked by optical microscopy and FE-SEM. As shown in Fig. 3(a), $NiTe_2$ grown at T_{syn} = 600 °C has arbitrarily shaped grains with small sizes of 1–3 μm, and the size of the $NiTe_2$ grains increases as increasing T_{syn} from 560 °C to 700 °C. The trend curve of grain size as a function of the synthetic temperature shows that the lateral size increases rapidly, indicating that the high-temperature synthesis aids the lateral growth of $NiTe_2$.

We confirmed the lateral 2D growth of the $NiTe_2$ grains using XRD

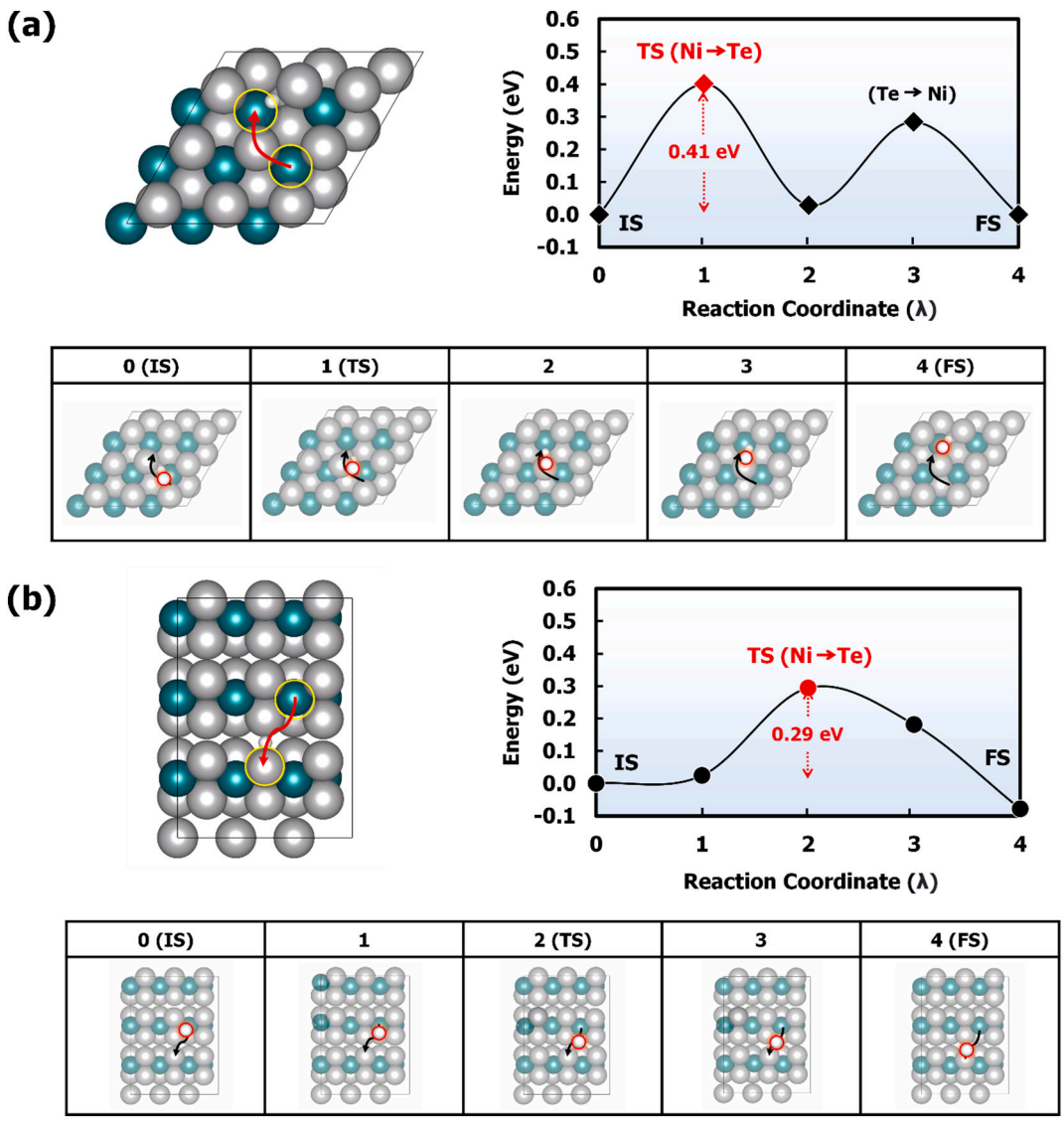


Fig. 2. (a) Minimum-energy pathway from Ni to Ni on the basal plane (001) and the corresponding energy barrier for the diffusion of an H atom on the basal plane (001). (b) Minimum-energy pathway from Ni to Te on the edge plane (100) and the corresponding energy barrier for the diffusion of an H atom on the edge plane (100). Ni, Te, and H atoms are presented in green, gray, and white, respectively.

measurement. As shown in Fig. 3(b), the XRD patterns are well-matched with the trigonal structure of 1 T, and no impurity peaks are observed. The Rietveld refinements show the lattice constants of $a = 3.8504$ Å and $c = 5.2612$ Å, consistent with the reported lattice constants of good stoichiometric $NiTe_2$. Moreover, an XRD peak corresponding to (00*n*) becomes stronger as Tsyn increases (see Fig. S2), indicating that the high-temperature synthesis of $NiTe_2$ leads to a preferential growth direction along the *c*-axis.

Fig. 3(c) shows that the as-prepared $NiTe_2$ exhibits an in-plane E_g Raman mode around 80.4 cm^{-1}. However, an out-of-plane A_{1g} Raman mode around 140.2 cm^{-1} has almost disappeared [36,59]. Using the scotch tape method, we also measure the Raman spectra of mechanically exfoliated $NiTe_2$ flakes on the SiO_2/Si substrate. Fig. S3 shows that the intensity of the Si peaks at 520 cm^{-1} coming from the SiO_2/Si substrate enables us to anticipate the relative thickness of the $NiTe_2$ flakes, thin (red line), thick (black line), and bulk (blue line) $NiTe_2$. Unlike the bulky $NiTe_2$, the exfoliated $NiTe_2$ exhibits two prominent Raman spectra, in-plane E_g Raman mode around 80.4 cm^{-1} and an out-of-plane A_{1g} Raman mode around 140.2 cm^{-1}. The intensity ratio of A_{1g} and E_g decreases from 0.40 to 0.12 as the thickness of $NiTe_2$ is consistent with the tendency of the intensity ratio (A_{1g}/E_g) found in the thickness-dependent Raman spectra of 1 T TMDs [60]. However, contrary to the reported tendency of thickness-dependent Raman in 1 T TMD, we observed that the E_g and A_{1g} Raman modes of 1 T $NiTe_2$ have been red-shifted by 1.5 cm^{-1} and 2.1 cm^{-1}, respectively. Qi et al. reported that the Eg Raman modes of 1 T $NiTe_2$ are sensitive to the external pressure. Therefore, the Eg Raman modes experience phonon hardening as the thickness increases [61].

The quantitative analysis of the $NiTe_2$ flakes is analyzed using EDS, showing that the $NiTe_2$ flakes have Ni and Te atoms, with the atomic ratio of Ni and Te being approximately 1:2 (see Fig. S4). The element mapping images of Si, Ni, and Te indicate the uniform distribution of Ni and Te in the $NiTe_2$ flake, as shown in Fig. 4(a). The high-magnification SEM images show that the $NiTe_2$ has a layered structure (see Fig. S5). We further study the chemical state of the $NiTe_2$ flakes grown on the SiO_2/Si substrate using XPS. The XPS survey in Fig. 4(b) shows that most elements are Ni, Te, Si, and O, and there are small amounts of carbon oxides. The valence band spectra of XPS in Fig. 4(c) show that $NiTe_2$ has a metallic character with a considerable density of states at the Fermi energy (E_F). The Ni *2p* and Te *3d* spectra have sharp, prominent peaks from $NiTe_2$ and small peaks related to Ni and Te oxides [59]. We summarize the XPS fitting parameters in Table S2.

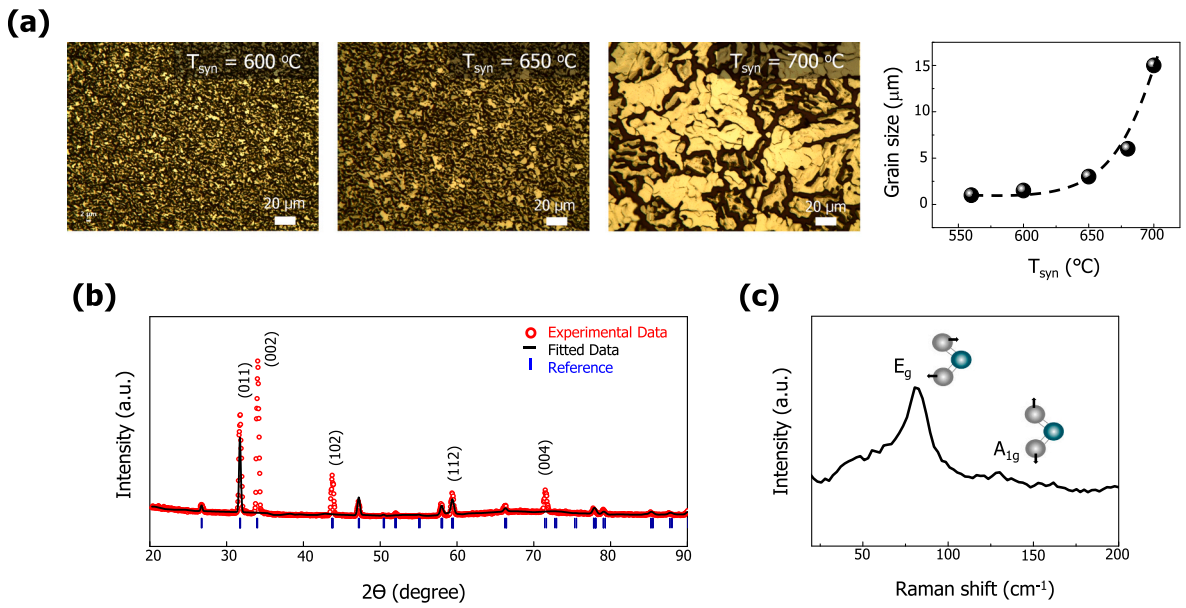


Fig. 3. (a) Optical microscopy images of $NiTe_2$ grown at 600 °C, 650 °C, and 700 °C and the trend curve of grain size as a function of synthetic temperature. (b) XRD patterns of the as-grown $NiTe_2$ with fitted data and reference bars. (c) Raman spectra of the synthesized $NiTe_2$ flakes.

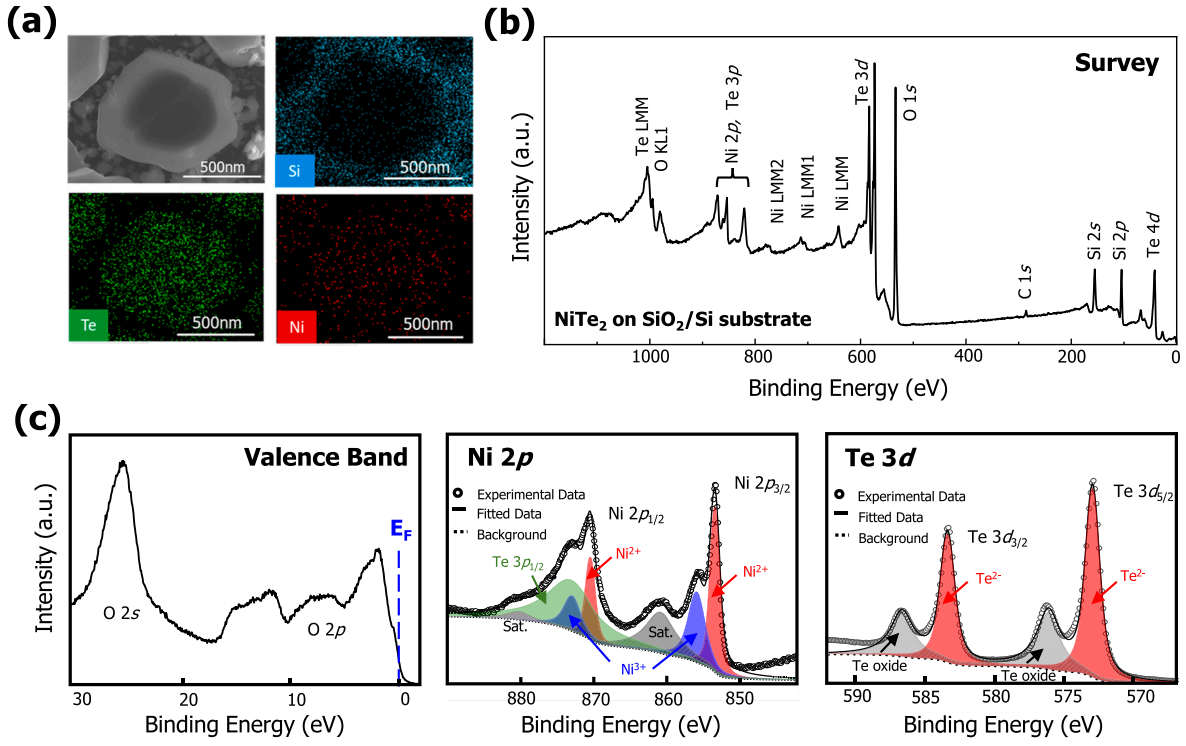


Fig. 4. (a) SEM and EDS images of the $NiTe_2$ flakes. (b) XPS survey of the $NiTe_2$ flakes on the SiO_2/Si substrate. (c) Valence band, Ni 2*p*, and Te 3*d* spectra of the $NiTe_2$ flakes on the SiO_2/Si substrate with fitted data.

To study the contribution of basal plane atoms and edge plane atoms for HER, experiments with an HER microreactor with three electrodes, reference (Ag/AgCl), counter (graphite rod), and working (Au) electrodes are implemented as shown in Fig. 5(a). The bumpy, sloped, and flat $NiTe_2$ flakes are transferred to the pre-patterned Au electrode in the HER microreactor and the $NiTe_2$ flakes are selectively opened as HER windows to the acidic electrolyte with the PMMA layer. The selected sample areas of bumpy (numbered as '1'), sloped (numbered as '2'), and flat (numbered as '3', '4') $NiTe_2$ flakes are marked with black squares (see Fig. 5(b)). Sample 1 probably contains many edge atoms because the $NiTe_2$ flake has a bumpy surface with many crystal orientations. In sample 2, there is an interference with a rainbow pattern at the surface of $NiTe_2$, indicating that light is reflected by the sloped sample [15]. Thus, sample 2 has many exposed edge atoms in the sloped surface of $NiTe_2$. On the other hand, samples 3 and 4 mainly have basal plane atoms with a small number of edge atoms in the HER windows because of their flat geometry.

The linear sweep voltammetry (LSV) curves of the $NiTe_2$ flakes are

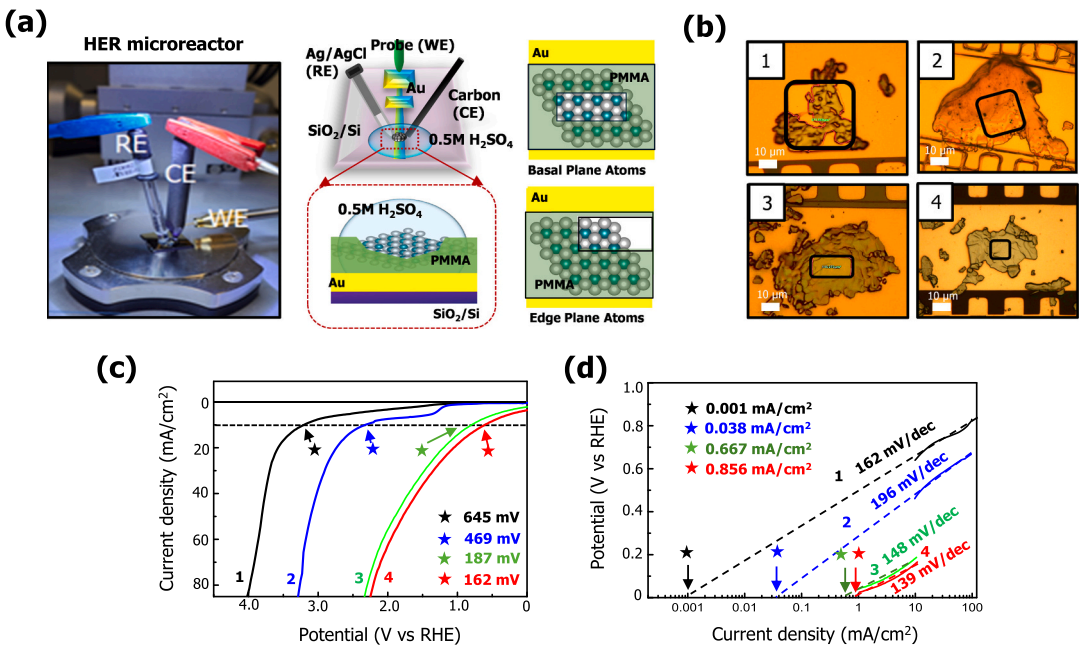


Fig. 5. (a) Experimental setup of the HER microreactor with three electrodes: WE, CE, and RE. $NiTe_2$ flakes were exfoliated on the patterned Au electrode and partially covered by PMMA. The desired sample areas with basal or edge plane atoms were selectively opened for the HER process. (b) Optical microscopy images and (c) LSV curves of four $NiTe_2$ flakes labeled 1, 2, 3, and 4, with different HER windows (marked with black squares). (d) Tafel slopes of $NiTe_2$ labeled 1 and 4.

measured with different sample morphologies, bumpy, sloped, and flat surfaces, as shown in Fig. 5(c). The overpotentials values of $NiTe_2$ with the current density of 10 mA/cm^2 are different: −0.645, −0.469, −0.187, and − 0.162 V for the sample 1, 2, 3, and 4, respectively. Interestingly, a high current density of >800 mA/cm^2 has been observed at the flat samples of $NiTe_2$ (see Fig. S6), which can be explained by the topological behaviors of the extremely large current density in recent studies of 2D catalysts [39–41]. Large Tafel slopes of 162, 196, 148, and 139 mV/dec are deduced from the LSV curves of samples 1, 2, 3, and 4, as shown in Fig. 5(d). The large Tafel slopes of $NiTe_2$ can be explained by the fact that the proton adsorption at the active sites (Volmer step) could be the rate-determining step because of the small HER windows during HER measurements with the HER microreactor.

Such HER activity of $NiTe_2$ with different HER windows could be attributed to the other active sites of $NiTe_2$, as described in Fig. 1(d), basal plane atoms, edge atoms, and vacant atomic sites. It has been reported that metallic TMDs have basal plane activity for HER [6,62,63]. Therefore, we hypothesize hydrogen conversion occurs at Te atoms on the $NiTe_2$ surface. We estimate the conversion rate from a proton to a hydrogen molecule of the basal plane Te atoms in the three HER windows. We calculate the turnover frequency (TOF) of a proton with equation, $TOF = \frac{j_0 \bullet N_A}{S \bullet n \bullet F}$, where j_0 is the exchange current density, n is the number of electrons transferred per molecule (2 for HER), F is the Faraday constant (96,458C·mol^{-1}), S is the active site density, and N_A is Avogadro's number (6.02 × 10^{23} mol^{-1}). The active site density (S) is calculated by counting the number of Te atoms at the topmost layer, 11.40 nm^{-2} and 7.79 nm^{-2} for the (100) and (001) planes of $NiTe_2$. The exchange current densities (j_0) at the potential of 0 V are taken from the LSV curves of samples 1, 2, 3, and 4 (see Fig. 5(d)); 0.001, 0.038, 0.667, and 0.856 mA/cm^2, respectively.

The detailed values for the calculation of TOF are summarized in Table 1. The estimated TOF values of $NiTe_2$ are 0.003, 0.104, 2.671, and 3.429 s^{-1} for samples 1, 2, 3, and 4, respectively. The flat $NiTe_2$ surfaces have larger TOF values than the bumpy and sloped $NiTe_2$ surface, indicating that the basal plane atoms have better HER activity than the edge plane atoms, which is inconsistent with our theoretical results.

The experimentally obtained TOFs of $NiTe_2$, 0.003–0.103 s^{-1} for edge plane atoms and 2.671–3.429 s^{-1} for basal plane atoms, seem to contradict our theoretical predictions, which showed that the edge plane atoms can convert protons into hydrogen molecules more effectively than the basal plane atoms. Considering that the Te vacancy creation can lower ΔG_{H^*} in $NiTe_2$, there might be more Te vacancies at the basal plane than at the edge plane. However, the calculated formation energies of Te vacancies at the basal plane are higher than the edge plane by 0.13 eV, 0.12 eV, and 0.09 eV for one, two, and three Te vacancies in $NiTe_2$, respectively. This indicates that the basal plane of $NiTe_2$ hardly has Te vacancies, which is consistent with our experimental characterization results: suitable stoichiometry and crystallinity of the basal plane are confirmed by XRD, EDS, Raman spectroscopy, and XPS.

Defunctionalized edge plane atoms by oxidation or degradation could also be considered to explain the controversy between the theoretical prediction and the experimental results. As the edge plane atoms could be more active than the basal plane atoms because of less-coordinated Ni atoms, edge plane atoms can be easily oxidized or deformed during HER in acidic environments. However, considering that the calculated ΔG_{H^*} values for $NiTe_2$ (see Fig. 1(e)) are consistently higher than those for other Ni-related catalysts [64,65], the basal and edge plane atoms of pristine $NiTe_2$ should be almost inactive for HER. Therefore, the observed high HER activity of the basal plane atoms in $NiTe_2$ is somewhat mysterious.

According to our approach with *d*-band theory, thermodynamic, and kinetic analyses, the edge plane has to be more active than the basal

Table 1
Summary of electrocatalytic activities observed in four different $NiTe_2$.

#	Overpotential (mV vs. RHE)	Tafel slope (mV/dec)	S (#/nm^2)	j_0 (mA/cm^2)	TOF (s^{-1})	Comments
#1	645	162	$11.40_{(100)}$	0.001	0.003	Edge-rich plane
#2	469	196	$11.40_{(100)}$	0.038	0.103	Edge plane
#3	187	148	$7.79_{(001)}$	0.667	2.671	Basal plane
#4	162	139	$7.79_{(001)}$	0.856	3.429	Basal plane

plane in $NiTe_2$. However, the experimental results showed extraordinary HER activity in the basal plane of $NiTe_2$. Therefore, we must consider an intriguing carrier transport originating from low-dimensionality beyond the *d*-band theory. Recently reported theoretical calculations confirmed that the dispersive bands composed mainly of Te 5*p* orbitals near the Fermi level strongly contribute to the topological surface states of $NiTe_2$, which can influence the carrier transport between the surface atoms of $NiTe_2$ and the approaching protons at the interface of the catalytic surface and the electrolyte [25,26]. As shown in Fig. 6, we analyze the band structure evolution of the $NiTe_2$ basal and edge plane surfaces upon hydrogen adsorption. We define the 2D Brillouin zone and the corresponding K-point path for the basal and edge planes. It has been reported that the topological states of Dirac semimetal efficiently transfer the electrons to the adsorbed hydrogen atoms, leading to an outstanding HER with a high value of TOF [6,14,66–68]. Our band structure analyses show that hydrogen adsorption on the basal and edge planes causes minimal changes in the band structure. In contrast, significant changes are induced by the hydrogen adsorption near E_F on the edge plane. In many Dirac semimetal catalysts, the hydrogen adsorption shifts the surface state bands above or below E_F because of the charge transfer between hydrogen and the catalyst surface [67,69,70].

Interestingly, the Dirac points of $NiTe_2$ are located at different energies with different crystal orientations, resulting in an anisotropic electronic band structure [71]. Therefore, the characteristic features of relativistic carrier transport could be resolved if the HER has been tested with different crystal orientations of $NiTe_2$. Recently, crystal-orientation-dependent catalytic activity has been reported in the topological catalysts, showing that topological states are responsible for catalytic activities [31,72,73]. Considering that the (001) surface of $NiTe_2$ has Dirac points near E_F, while the Dirac points of the (100) surface of NiTe2 are far from EF [25,26], the basal plane of NiTe2 can show an outstanding HER performance even though there are contradictory theoretical predictions. The electronic structure of $NiTe_2$ also exhibits one Dirac point along Γ-A direction, which corresponds to the *c*-axis of $NiTe_2$. It indicates that the Dirac fermions with high carrier mobility (300–400 $cm^2/V{\cdot}s$ [25]) can contribute to the HER of the (001) surface of $NiTe_2$ and show outstanding HER performance. Therefore, the high HER activity observed at the basal plane of $NiTe_2$ might have originated from the outstanding carrier transport of Dirac fermions, which probably provides a new concept of topological catalysts.

4. Conclusion

We demonstrate the anisotropy of HER activity in a possible type II Dirac semimetal $NiTe_2$. The HER activities of basal and edge plane atoms have been compared theoretically using DFT calculations and experimentally using atomic-level analysis with the HER microreactor. Our electronic structure analyses based on the *d*-band theory, which has been accepted for many 3*d* and 4*d* metal catalysts, show that less-coordinated Ni atoms at the edge plane could be major active sites for

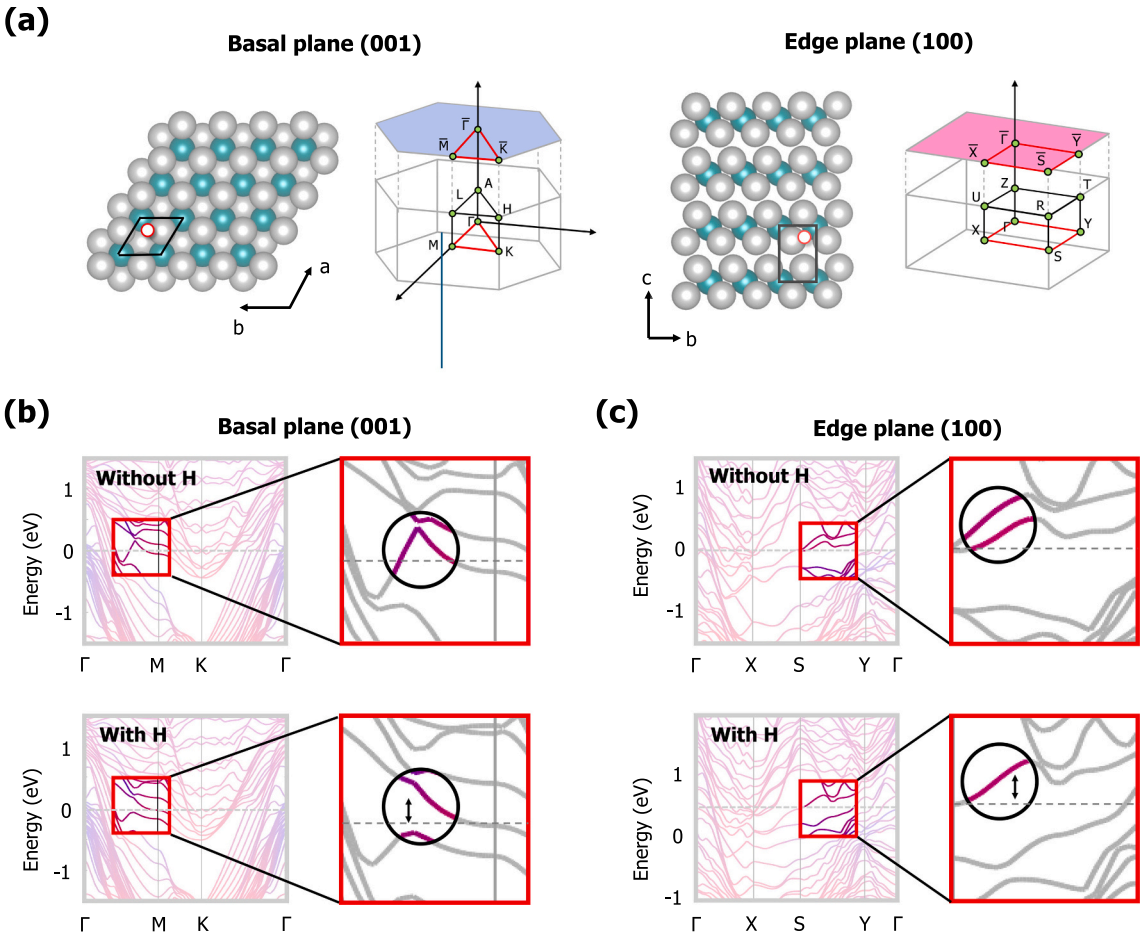


Fig. 6. (a) The Brillouin zone for the basal plane (001) corresponds to the basal surface with a hexagonal structure, where the K-path follows the sequence *Γ*–M–K–*Γ*. The Brillouin zone for the edge plane (100) corresponds to the edge surface with an orthorhombic structure, and the K-path follows the sequence *Γ*–X–S–Y–*Γ*. Ni, Te, and H atoms are denoted in green, gray, and white, respectively. The band structure of (b) the basal plane (001) and (c) the edge plane (100) without and with an adsorbed H atom. Changes in the band structure near the Fermi level are highlighted with red boxes, and the *d* orbital of the Ni atom and the *p* orbital of the Te atom are denoted in red and blue, respectively.

HER. Subsequent DFT calculations suggest that $NiTe_2$ edge plane surfaces are more favorable for the HER than the basal plane surfaces, both kinetically and thermodynamically. However, our electrochemical measurements with the HER microreactor reveal that the basal plane of $NiTe_2$ shows better catalytic activity than the $NiTe_2$ edge. This indicates that the basal plane atoms are more active than edge atoms, which is inconsistent with our theoretical predictions. We claimed that the high basal plane of $NiTe_2$ with high current density could originate from significant contributions of Dirac fermions located near the Fermi level, and the carrier transport could be enhanced between the active site atoms and the approaching proton at the interface. Therefore, the different contributions of Dirac fermions to the carrier transport at the interface lead to the anisotropic behavior of the HER activity. Our studies demonstrate abnormal catalytic activity at the $NiTe_2$ surface, which opens a new era of topological catalysts for next-generation energy conversion.

CRediT authorship contribution statement

Seung Weon Jeong: Writing – original draft, Resources, Methodology, Investigation, Formal analysis, Data curation, Conceptualization. **Jeong Hyo Kim:** Writing – original draft, Resources, Methodology, Investigation, Formal analysis, Data curation, Conceptualization. **Seungyeon Lee:** Methodology, Conceptualization. **Hyeonju Kim:** Data curation, Methodology. **Hee Jung Park:** Data curation, Methodology. **Heejun Yang:** Writing – review & editing, Validation, Supervision. **Sangheon Lee:** Writing – review & editing, Validation, Supervision, Resources, Project administration, Methodology, Funding acquisition. **Suyeon Cho:** Writing – review & editing, Validation, Supervision, Project administration, Methodology, Funding acquisition.

Declaration of competing interest

The authors declare that they have no known competing financial interests or personal relationships that could have appeared to influence the work reported in this paper.

Acknowledgments

Suyeon Cho acknowledges support from the Basic Science Research Program through the National Research Foundation of Korea (NRF), funded by the Ministry of Science, ICT and Future Planning under Grant No. NRF-2025-00514456 and RS-2025-02982993. Sangheon Lee acknowledges support from the National Research Foundation of Korea, funded by the Ministry of Science, ICT and Future Planning (No. NRF-2023R1A2C1006648). Heejun Yang acknowledges support from the National Research Foundation of Korea, funded by the Ministry of Science and ICT (RS-2024-00340377). Hee Jung Park acknowledges support from the Korea Basic Science Institute under the R & D Program funded by the Ministry of Science and ICT (No. C513550).

Appendix A. Supplementary data

Supplementary data to this article can be found online at https://doi.org/10.1016/j.cej.2025.164789.

Data availability

Data will be made available on request.

References

[1] J. Zhang, X. Yang, C. Chen, Y. Li, J. Li, W. Chen, Y. Cui, X.a. Li, X. Zhu, Surface phosphorus grafting of $Ti_3C_2T_x$ MXene as an interface charge “bridge” for efficient electrocatalytic hydrogen evolution in all-pH media, Chem. Mater. 36 (24) (2024) 12006–12017, https://doi.org/10.1021/acs.chemmater.4c02831.

[2] J. Li, J. Zhang, J. Shen, H. Wu, H. Chen, C. Yuan, N. Wu, G. Liu, D. Guo, X. Liu, Self-supported electrocatalysts for the hydrogen evolution reaction, Materials Chemistry Frontiers 7 (4) (2023) 567–606, https://doi.org/10.1039/D2QM00931E.

[3] J. Li, J. Zhang, J. Zhang, K. Pan, H. Xu, H. Chen, G. Liu, N. Wu, C. Yuan, X. Liu, Tailoring supports for enhancing the electrocatalytic hydrogen evolution performance of platinum species: a review, J. Mater. Chem. A 11 (37) (2023) 19812–19844, https://doi.org/10.1039/D3TA04199A.

[4] J. Li, B. Li, H. Huang, S. Yan, C. Yuan, N. Wu, D. Guo, X. Liu, Polyvinylpyrrolidone gel based $Pt/Ni(OH)_2$ heterostructures with redistributing charges for enhanced alkaline hydrogen evolution reaction, J. Mater. Chem. A 9 (47) (2021) 27061–27071, https://doi.org/10.1039/D1TA06149F.

[5] J. Azadmanjiri, V.K. Srivastava, P. Kumar, Z. Sofer, J. Min, J. Gong, Graphene-supported 2D transition metal dichalcogenide van der Waals heterostructures, Appl. Mater. Today 19 (2020) 100600.

[6] J. Seok, J.-H. Lee, S. Cho, B. Ji, H.W. Kim, M. Kwon, D. Kim, Y.-M. Kim, S.H. Oh, S. W. Kim, Active hydrogen evolution through lattice distortion in metallic $MoTe_2$, 2D Materials 4 (2) (2017) 025061.

[7] Y. Sui, J. Zhou, X. Wang, L. Wu, S. Zhong, Y. Li, Recent advances in black-phosphorus-based materials for electrochemical energy storage, Mater. Today 42 (2021) 117–136, https://doi.org/10.1016/j.mattod.2020.09.005.

[8] X. Qi, Y. Zhang, Q. Ou, S.T. Ha, C.W. Qiu, H. Zhang, Y.B. Cheng, Q. Xiong, Q. Bao, Photonics and optoelectronics of 2D metal-halide perovskites, Small 14 (31) (2018) 1800682.

[9] J. Li, N. Wu, J. Zhang, H.-H. Wu, K. Pan, Y. Wang, G. Liu, X. Liu, Z. Yao, Q. Zhang, Machine learning-assisted low-dimensional electrocatalysts design for hydrogen evolution reaction, Nano-Micro Letters 15 (1) (2023) 227, https://doi.org/10.1007/s40820-023-01192-5.

[10] J. Li, M. Zhou, H.-H. Wu, L. Wang, J. Zhang, N. Wu, K. Pan, G. Liu, Y. Zhang, J. Han, X. Liu, X. Chen, J. Wan, Q. Zhang, Machine learning-assisted property prediction of solid-state electrolyte, Adv. Energy Mater. 14 (20) (2024) 2304480, https://doi.org/10.1002/aenm.202304480.

[11] R. Xie, T. Zhang, H. Weng, G.-L. Chai, Progress, advantages, and challenges of topological material catalysts, Small Science 2 (4) (2022) 2100106.

[12] M. Li, Z. He, L. Jin, L. Wang, Y. Liu, G. Liu, X. Zhang, Synergistic boost of catalytic activity in ZrTe topological catalyst via multiple topologically-electronic states, Appl. Surf. Sci. 648 (2024) 159081.

[13] Z. Li, Z. He, L. Wang, W. Meng, X. Dai, G. Liu, Y. Liu, X. Zhang, High-performance hydrogen evolution reaction in quadratic nodal line semimetal Na2CdSn, iScience 27 (2024) 110708, https://doi.org/10.1016/j.isci.2024.110708.

[14] C.R. Rajamathi, U. Gupta, N. Kumar, H. Yang, Y. Sun, V. Suss, C. Shekhar, M. Schmidt, H. Blumtritt, P. Werner, B. Yan, S. Parkin, C. Felser, C.N.R. Rao, Weyl semimetals as hydrogen evolution catalysts, Adv. Mater. 29 (19) (2017), https://doi.org/10.1002/adma.201606202.

[15] Y. Wang, Y. Li, Z. Chen, Not your familiar two dimensional transition metal disulfide: structural and electronic properties of the PdS_2 monolayer, J. Mater. Chem. C 3 (37) (2015) 9603–9608.

[16] L.-J. Ma, H. Shen, Activating $PtSe_2$ monolayer for hydrogen evolution reaction by defect engineering and Pd doping, Appl. Surf. Sci. 545 (2021) 149013, https://doi.org/10.1016/j.apsusc.2021.149013.

[17] C. Long, Y. Liang, H. Jin, B. Huang, Y. Dai, $PdSe_2$: flexible two-dimensional transition metal dichalcogenides monolayer for water splitting photocatalyst with extremely low recombination rate, ACS Applied Energy Materials 2 (1) (2018) 513–520.

[18] X. Chia, Z. Sofer, J. Luxa, M. Pumera, Layered noble metal dichalcogenides: tailoring electrochemical and catalytic properties, ACS Appl. Mater. Interfaces 9 (30) (2017) 25587–25599, https://doi.org/10.1021/acsami.7b05083.

[19] N. Cheng, Q. Liu, A.M. Asiri, W. Xing, X. Sun, A Fe-doped Ni_3S_2 particle film as a high-efficiency robust oxygen evolution electrode with very high current density, J. Mater. Chem. A 3 (46) (2015) 23207–23212.

[20] P. Chen, T. Zhou, M. Zhang, Y. Tong, C. Zhong, N. Zhang, L. Zhang, C. Wu, Y. Xie, 3D nitrogen-anion-decorated nickel sulfides for highly efficient overall water splitting, Adv. Mater. 29 (30) (2017) 1701584.

[21] L. Yang, H. Xu, H. Liu, D. Cheng, D. Cao, Active site identification and evaluation criteria of in situ grown CoTe and NiTe nanoarrays for hydrogen evolution and oxygen evolution reactions, Small Methods 3 (5) (2019) 1900113, https://doi.org/10.1002/smtd.201900113.

[22] Y. Li, X. He, M. Guo, D. Lin, C. Xu, F. Xie, X. Sun, Porous $NiTe_2$ nanosheet array: an effective electrochemical sensor for glucose detection, Sensors Actuators B Chem. 274 (2018) 427–432, https://doi.org/10.1016/j.snb.2018.07.172.

[23] S. Chen, B. Wu, H. Qian, Z. Wu, P. Liu, F. Li, H. He, J. Wu, B. Liu, An asymmetric supercapacitor using sandwich-like NiS/NiTe/Ni positive electrode exhibits a super-long cycle life exceeding 200,000 cycles, J. Power Sources 438 (2019) 227000, https://doi.org/10.1016/j.jpowsour.2019.227000.

[24] P. Zhou, L. Fan, J. Wu, C. Gong, J. Zhang, Y. Tu, Facile hydrothermal synthesis of NiTe and its application as positive electrode material for asymmetric supercapacitor, J. Alloys Compd. 685 (2016) 384–390, https://doi.org/10.1016/j.jallcom.2016.05.287.

[25] C. Xu, B. Li, W. Jiao, W. Zhou, B. Qian, R. Sankar, N.D. Zhigadlo, Y. Qi, D. Qian, F.-C. Chou, Topological type-II Dirac fermions approaching the Fermi level in a transition metal dichalcogenide $NiTe_2$, Chem. Mater. 30 (14) (2018) 4823–4830.

[26] S. Mukherjee, S.W. Jung, S.F. Weber, C. Xu, D. Qian, X. Xu, P.K. Biswas, T.K. Kim, L.C. Chapon, M.D. Watson, Fermi-crossing Type-II Dirac fermions and topological surface states in $NiTe_2$, Sci. Rep. 10 (1) (2020) 12957.

[27] F. Zheng, X.-B. Li, P. Tan, Y. Lin, L. Xiong, X. Chen, J. Feng, Emergent superconductivity in two-dimensional $NiTe_2$ crystals, Phys. Rev. B 101 (10) (2020) 100505.

[28] J. Shen, H. Xing, L. Wang, Z. Hu, L. Zhang, X. Wang, Z. Chen, C. Yao, M. Jiang, F. Fei, A van der Waals heterostructure based on nickel telluride and graphene with spontaneous high-frequency photoresponse, Appl. Phys. Lett. 120 (6) (2022).

[29] Q. Liu, F. Fei, B. Chen, X. Bo, B. Wei, S. Zhang, M. Zhang, F. Xie, M. Naveed, X. Wan, Nontopological origin of the planar Hall effect in the type-II Dirac semimetal $NiTe_2$, Phys. Rev. B 99 (15) (2019) 155119.

[30] J. Shi, Y. Huan, M. Xiao, M. Hong, X. Zhao, Y. Gao, F. Cui, P. Yang, S.J. Pennycook, J. Zhao, Two-dimensional metallic $NiTe_2$ with ultrahigh environmental stability, conductivity, and electrocatalytic activity, ACS Nano 14 (7) (2020) 9011–9020.

[31] X. Zhang, L. Wang, M. Li, W. Meng, Y. Liu, X. Dai, G. Liu, Y. Gu, J. Liu, L. Kou, Topological surface state: universal catalytic descriptor in topological catalysis, Mater. Today 67 (2023) 23–32, https://doi.org/10.1016/j.mattod.2023.05.002.

[32] A.Y.S. Eng, J.L. Cheong, S.S. Lee, Controlled synthesis of transition metal disulfides (MoS_2 and WS_2) on carbon fibers: effects of phase and morphology toward lithium–sulfur battery performance, Appl. Mater. Today 16 (2019) 529–537, https://doi.org/10.1016/j.apmt.2019.07.009.

[33] S. Wang, D. Zhang, B. Li, C. Zhang, Z. Du, H. Yin, X. Bi, S. Yang, Ultrastable in-plane 1T–2H MoS_2 heterostructures for enhanced hydrogen evolution reaction, Adv. Energy Mater. 8 (25) (2018) 1801345.

[34] D. Edelberg, D. Rhodes, A. Kerelsky, B. Kim, J. Wang, A. Zangiabadi, C. Kim, A. Abhinandan, J. Ardelean, M. Scully, Approaching the intrinsic limit in transition metal diselenides via point defect control, Nano Lett. 19 (7) (2019) 4371–4379.

[35] X. Chia, Z. Sofer, J. Luxa, M. Pumera, Unconventionally layered $CoTe_2$ and $NiTe_2$ as electrocatalysts for hydrogen evolution, Chem. Eur. J. 23 (48) (2017) 11719–11726.

[36] S. Nappini, D.W. Boukhvalov, G. D'Olimpio, L. Zhang, B. Ghosh, C.N. Kuo, H. Zhu, J. Cheng, M. Nardone, L. Ottaviano, Transition-metal dichalcogenide $NiTe_2$: an ambient-stable material for catalysis and nanoelectronics, Adv. Funct. Mater. 30 (22) (2020) 2000915.

[37] Z. Wang, L. Zhang, Nickel ditelluride nanosheet arrays: a highly efficient electrocatalyst for the oxygen evolution reaction, ChemElectroChem 5 (8) (2018) 1153–1158, https://doi.org/10.1002/celc.201701357.

[38] Z. Wang, P. Guo, M. Liu, C. Guo, H. Liu, S. Wei, J. Zhang, X. Lu, Rational design of metallic $NiTe_x$ (x = 1 or 2) as bifunctional electrocatalysts for efficient urea conversion, ACS Applied Energy Materials 2 (5) (2019) 3363–3372.

[39] C. Tang, H.F. Wang, X. Chen, B.Q. Li, T.Z. Hou, B. Zhang, Q. Zhang, M.M. Titirici, F. Wei, Topological defects in metal-free nanocarbon for oxygen electrocatalysis, Adv. Mater. 28 (32) (2016) 6845–6851.

[40] M. Yan, H. Huang, K. Zhang, E. Wang, W. Yao, K. Deng, G. Wan, H. Zhang, M. Arita, H. Yang, Lorentz-violating type-II Dirac fermions in transition metal dichalcogenide $PtTe_2$, Nat. Commun. 8 (1) (2017) 257.

[41] H.-J. Noh, J. Jeong, E.-J. Cho, K. Kim, B. Min, B.-G. Park, Experimental realization of type-II Dirac fermions in a $PdTe_2$ superconductor, Phys. Rev. Lett. 119 (1) (2017) 016401.

[42] J.P. Perdew, K. Burke, M. Ernzerhof, Generalized gradient approximation made simple, Phys. Rev. Lett. 77 (18) (1996) 3865.

[43] G. Kresse, J. Furthmüller, Efficient iterative schemes for ab initio total-energy calculations using a plane-wave basis set, Phys. Rev. B 54 (16) (1996) 11169.

[44] G. Henkelman, B.P. Uberuaga, H. Jónsson, A climbing image nudged elastic band method for finding saddle points and minimum energy paths, J. Chem. Phys. 113 (22) (2000) 9901–9904.

[45] J.K. Nørskov, T. Bligaard, A. Logadottir, J. Kitchin, J.G. Chen, S. Pandelov, U. Stimming, Trends in the exchange current for hydrogen evolution, J. Electrochem. Soc. 152 (3) (2005) J23.

[46] A.A. Gokhale, J.A. Dumesic, M. Mavrikakis, On the mechanism of low-temperature water gas shift reaction on copper, J. Am. Chem. Soc. 130 (4) (2008) 1402–1414.

[47] L.S. Banu, V. Veerapandy, H. Fjellvåg, P. Vajeeston, First-principles insights into the relative stability, physical properties, and chemical properties of $MoSe_2$, ACS Omega 8 (15) (2023) 13799–13812, https://doi.org/10.1021/acsomega.2c08217.

[48] O.J. Clark, F. Mazzola, I. Marković, J.M. Riley, J. Feng, B.J. Yang, K. Sumida, T. Okuda, J. Fujii, I. Vobornik, T.K. Kim, K. Okawa, T. Sasagawa, M.S. Bahramy, P. D.C. King, A general route to form topologically-protected surface and bulk Dirac fermions along high-symmetry lines, Electronic Structure 1 (1) (2019), https://doi.org/10.1088/2516-1075/ab09b7.

[49] V.D. Esin, O.O. Shvetsov, A.V. Timonina, N.N. Kolesnikov, E.V. Deviatov, Interface superconductivity in a Dirac semimetal $NiTe_2$, Nanomaterials (Basel) 12 (23) (2022), https://doi.org/10.3390/nano12234114.

[50] P.P. Ferreira, A.L.R. Manesco, T.T. Dorini, L.E. Correa, G. Weber, A.J.S. Machado, L.T.F. Eleno, Strain engineering the topological type-II Dirac semimetal $NiTe_2$, Phys. Rev. B 103 (12) (2021), https://doi.org/10.1103/PhysRevB.103.125134.

[51] J. Zhang, G.Q. Huang, The superconductivity and topological surface state of type-II Dirac semimetal $NiTe_2$, J. Phys. Condens. Matter 32 (20) (2020) 205702, https://doi.org/10.1088/1361-648X/ab6f84.

[52] M.S. Bahramy, O.J. Clark, B.J. Yang, J. Feng, L. Bawden, J.M. Riley, I. Markovic, F. Mazzola, V. Sunko, D. Biswas, S.P. Cooil, M. Jorge, J.W. Wells, M. Leandersson, T. Balasubramanian, J. Fujii, I. Vobornik, J.E. Rault, T.K. Kim, M. Hoesch, K. Okawa, M. Asakawa, T. Sasagawa, T. Eknapakul, W. Meevasana, P.D.C. King, Ubiquitous formation of bulk Dirac cones and topological surface states from a single orbital manifold in transition-metal dichalcogenides, Nat. Mater. 17 (1) (2018) 21–28, https://doi.org/10.1038/nmat5031.

[53] S. Lee, J. Cho, J.H. Jang, J. Han, S.P. Yoon, S.W. Nam, T.H. Lim, H.C. Ham, Impact of d-band occupancy and lattice contraction on selective hydrogen production from formic acid in the bimetallic Pd_3M (M=early transition 3d metals) catalysts, ACS Catal. 6 (1) (2016) 134–142.

[54] M.G. de Chialvo, A. Chialvo, Hydrogen evolution reaction: analysis of the Volmer-Heyrovsky-Tafel mechanism with a generalized adsorption model, J. Electroanal. Chem. 372 (1–2) (1994) 209–223.

[55] B. Conway, G. Jerkiewicz, Relation of energies and coverages of underpotential and overpotential deposited H at Pt and other metals to the 'volcano curve' for cathodic H_2 evolution kinetics, Electrochim. Acta 45 (25–26) (2000) 4075–4083.

[56] S.B. Pillai, B.A. Baraiya, D. Upadhyay, V. Mankad, P.K. Jha, Catalytic activity and underlying atomic rearrangement in monolayer CoOOH towards HER and OER, Int. J. Hydrog. Energy 45 (44) (2020) 23900–23907.

[57] R. Parsons, The rate of electrolytic hydrogen evolution and the heat of adsorption of hydrogen, Trans. Faraday Soc. 54 (1958) 1053–1063.

[58] P. Quaino, F. Juarez, E. Santos, W. Schmickler, Volcano plots in hydrogen electrocatalysis–uses and abuses, Beilstein J. Nanotechnol. 5 (1) (2014) 846–854.

[59] Y. Je, E. Kim, N.V. Binh, H. Kim, S.-Y. Cho, D.-H. Lee, M.J. Kwon, M. Choi, J.H. Lee, W.H. Nam, Analysis of physical and electrical properties of $NiTe_2$ single crystal grown via molten salt flux method, Electron. Mater. Lett. 19 (5) (2023) 452–461.

[60] M. Yan, E. Wang, X. Zhou, G. Zhang, H. Zhang, K. Zhang, W. Yao, N. Lu, S. Yang, S. Wu, High quality atomically thin $PtSe_2$ films grown by molecular beam epitaxy, 2D Materials 4 (4) (2017) 045015.

[61] M. Qi, C. An, Y. Zhou, H. Wu, B. Zhang, C. Chen, Y. Yuan, S. Wang, Y. Zhou, X. Chen, R. Zhang, Z. Yang, Pressure-driven Lifshitz transition in type-II Dirac semimetal $NiTe_2$, Phys. Rev. B 101 (11) (2020) 115124, https://doi.org/10.1103/PhysRevB.101.115124.

[62] H. Kwon, D. Bae, H. Jun, B. Ji, D. Won, J.-H. Lee, Y.-W. Son, H. Yang, S. Cho, Basal-plane catalytic activity of layered metallic transition metal ditellurides for the hydrogen evolution reaction, Appl. Sci. 10 (9) (2020) 3087.

[63] H. Kwon, B. Ji, D. Bae, J.-H. Lee, H.J. Park, Y.-M. Kim, Y.-W. Son, H. Yang, S. Cho, Role of anionic vacancy for active hydrogen evolution in WTe_2, Appl. Surf. Sci. 515 (2020) 145972.

[64] Y.-Y. Ma, Z.-L. Lang, L.-K. Yan, Y.-H. Wang, H.-Q. Tan, K. Feng, Y.-J. Xia, J. Zhong, Y. Liu, Z.-H. Kang, Highly efficient hydrogen evolution triggered by a multi-interfacial Ni/WC hybrid electrocatalyst, Energy Environ. Sci. 11 (8) (2018) 2114–2123.

[65] G. Ma, P. Guo, S. Wang, Y. Liu, Y. Xin, H. Li, R. Chen, A. Wang, One-step plasma nitriding synthesis of Ni_xN/NF (x=3, 4) for efficient hydrogen evolution, Appl. Surf. Sci. 561 (2021) 149972.

[66] Q. Xu, G. Li, Y. Zhang, Q. Yang, Y. Sun, C. Felser, Descriptor for hydrogen evolution catalysts based on the bulk band structure effect, ACS Catal. 10 (9) (2020) 5042–5048, https://doi.org/10.1021/acscatal.9b05539.

[67] Q. Yang, G. Li, K. Manna, F. Fan, C. Felser, Y. Sun, Topological engineering of Pt-group-metal-based chiral crystals toward high-efficiency hydrogen evolution catalysts, Adv. Mater. 32 (14) (2020) e1908518, https://doi.org/10.1002/adma.201908518.

[68] Y. Zhang, K.E. Arpino, Q. Yang, N. Kikugawa, D.A. Sokolov, C.W. Hicks, J. Liu, C. Felser, G. Li, Observation of a robust and active catalyst for hydrogen evolution under high current densities, Nat. Commun. 13 (1) (2022) 7784, https://doi.org/10.1038/s41467-022-35464-2.

[69] G. Li, C. Fu, W. Shi, L. Jiao, J. Wu, Q. Yang, R. Saha, M.E. Kamminga, A. K. Srivastava, E. Liu, A.N. Yazdani, N. Kumar, J. Zhang, G.R. Blake, X. Liu, M. Fahlman, S. Wirth, G. Auffermann, J. Gooth, S. Parkin, V. Madhavan, X. Feng, Y. Sun, C. Felser, Dirac nodal arc semimetal $PtSn_4$: an ideal platform for understanding surface properties and catalysis for hydrogen evolution, Angew. Chem. Int. Ed. Eng. 58 (37) (2019) 13107–13112, https://doi.org/10.1002/anie.201906109.

[70] W. Liu, X. Zhang, W. Meng, Y. Liu, X. Dai, G. Liu, Theoretical realization of hybrid Weyl state and associated high catalytic performance for hydrogen evolution in NiSi, iScience 25 (1) (2022) 103543, https://doi.org/10.1016/j.isci.2021.103543.

[71] M. Nurmamat, S.V. Eremeev, X. Wang, T. Yoshikawa, T. Kono, M. Kakoki, T. Muro, Q. Jiang, Z. Sun, M. Ye, Bulk Dirac cone and highly anisotropic electronic structure of $NiTe_2$, Phys. Rev. B 104 (15) (2021) 155133.

[72] Z. He, L. Wang, Y. Liu, Z. Li, X. Dai, G. Liu, X. Zhang, Nodal chain semimetal Co_2MnGa: a magnetic catalyst with topological significance, Chem. Eng. J. 481 (2024), https://doi.org/10.1016/j.cej.2023.148123.

[73] K. Wang, L. Li, P. Yu, N. Tang, L. Zeng, K. Li, C. Zhang, R. Chen, Z. Xiang, H. Wang, Y. Cai, K. Yan, H. Luo, Revealing the nontrivial topological surface states of catalysts for effective photochemical carbon dioxide conversion, Applied Catalysis B: Environment and Energy 358 (2024), https://doi.org/10.1016/j.apcatb.2024.124428.